

Supporting information for

“Tuning Topological Spin Textures in Size-Tailored Chiral Magnet Insulator Particles”

Priya R. Baral^{a,b}, Victor Ukleev^c, Thomas LaGrange^d, Robert Cubitt^e, Ivica Živković^f, Henrik M. Rønnow^f, Jonathan S. White^c, Arnaud Magrez^{a,}*

a) Crystal Growth Facility, Institute of Physics, École Polytechnique Fédérale de Lausanne (EPFL), CH-1015 Lausanne, Switzerland

b) Chair of Computational Condensed Matter Physics, Institute of Physics, École Polytechnique Fédérale de Lausanne (EPFL), CH-1015 Lausanne, Switzerland

c) Laboratory for Neutron Scattering and Imaging (LNS), Paul Scherrer Institut (PSI), CH-5232 Villigen, Switzerland

d) Laboratory for Ultrafast Microscopy and Electron Scattering (LUMES), Institute of Physics, École Polytechnique Fédérale de Lausanne (EPFL), CH-1015 Lausanne, Switzerland

e) Institut Laue Langevin, Large Scale Structures, 71 Avenue des Martyrs CS 20156, 38042 Grenoble, France

f) Laboratory for Quantum Magnetism, Institute of Physics, École Polytechnique Fédérale de Lausanne (EPFL), CH-1015 Lausanne, Switzerland

** Email : arnaud.magrez@epfl.ch*

Chemistry of Cu_2OSeO_3 particles. In order to validate the mechanism of conversion of $\text{CuSeO}_3 \cdot 2\text{H}_2\text{O}$ into Cu_2OSeO_3 , high temporal resolution (0.5 second for each pattern) XRD measurements were performed at SNBL, ESRF (Fig. S1A).

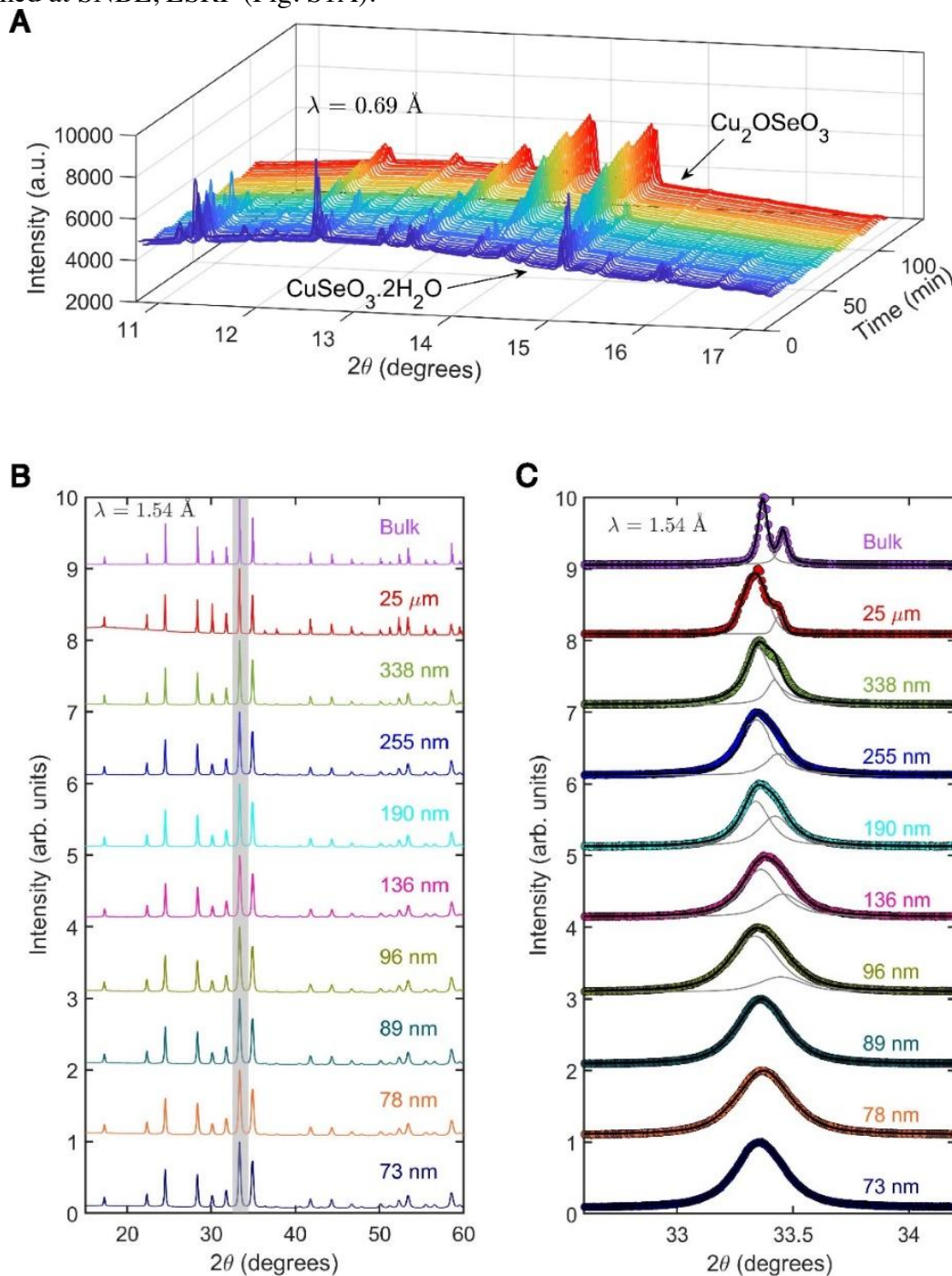


Fig. S1. (A) High resolution synchrotron XRD patterns of *in situ* transformation between the precursor $\text{CuSeO}_3 \cdot 2\text{H}_2\text{O}$ and final product Cu_2OSeO_3 , performed at SNBL, ESRF. This solid-solid transformation excludes the possibility of having any impurity phases throughout the whole process including the final Cu_2OSeO_3 phase. (B) High-resolution room temperature XRD patterns of all the particles, compared with that of the bulk sample. All specimens appear to be phase pure. (C) From the complete 2θ range, one peak at $2\theta \sim 33.4$ degrees has been singled out for all the particles and fitted with two Pseudo-Voigt functions for $\text{Cu-K}_{\alpha 1}$ and $\text{Cu-K}_{\alpha 2}$. In the bulk sample two independent functions are needed in order to have a reasonable fit. Whereas for the smallest particles, single Pseudo-Voigt function is sufficient in order to have an adequate fit, displaying the direct consequences of size broadening on the diffraction peaks.

In the presence of a basic medium as NH_4OH , $\text{CuSeO}_3 \cdot 2\text{H}_2\text{O}$ transforms completely to Cu_2OSeO_4 , with no trace of any other impurity phase(s). It provides us with great insight into the microscopic mechanism of formation of the final product. But this is beyond the scope of this work and will be reported somewhere else. The first insight into the size control of the particles is evident from the room-temperature XRD patterns (Fig. S1B & C). The evidence of peak broadening is obvious from here. In theory, this peak broadening can be a result of various factors, such as dislocations, twinning, coherency strain, chemical heterogeneity and, finally, small crystallite sizes. If these factors, other than the last one, were responsible for the observations, it would also be evident from other local characterization tools (Fig. 2E & F of the main text). Moreover, presence of atomistic crystalline defects may prevent the formation of a skyrmion, a highly symmetric object. And finally, since the instrumental contribution was fixed for all the patterns, the broadening of diffraction peaks is thus attributed to average coherent size of the particles.

Particle size determination. In our work, the particle size was determined by using a combination of dynamic light scattering (DLS), SEM imaging and Williamson-Hall analysis. As shown in the SEM image below, the as-grown sample is typically synthesized as agglomerates of well faceted and highly crystalline particles. Thus, the whole procedure was divided into two steps. In the first step, the secondary particle size was determined by DLS technique. The powder sample was suspended in a water + surfactant solution (SDS - Sodium Dodecyl Sulfate), followed by thorough sonication. The measurement was performed in a Zetasizer and for consistency check, 10-15 repetitions were performed for each sample size. As can be seen from the figure below, the DLS technique correctly measures the secondary particle sizes, for all samples. The example shown below corresponds to the one with mean size of 1324 ± 5 nm. The measurements confirm the very narrow distribution of the secondary particle size as opposed to the distribution reported so far in Holt *et al.*, Mater. Res. Express 8 116101 (2021).

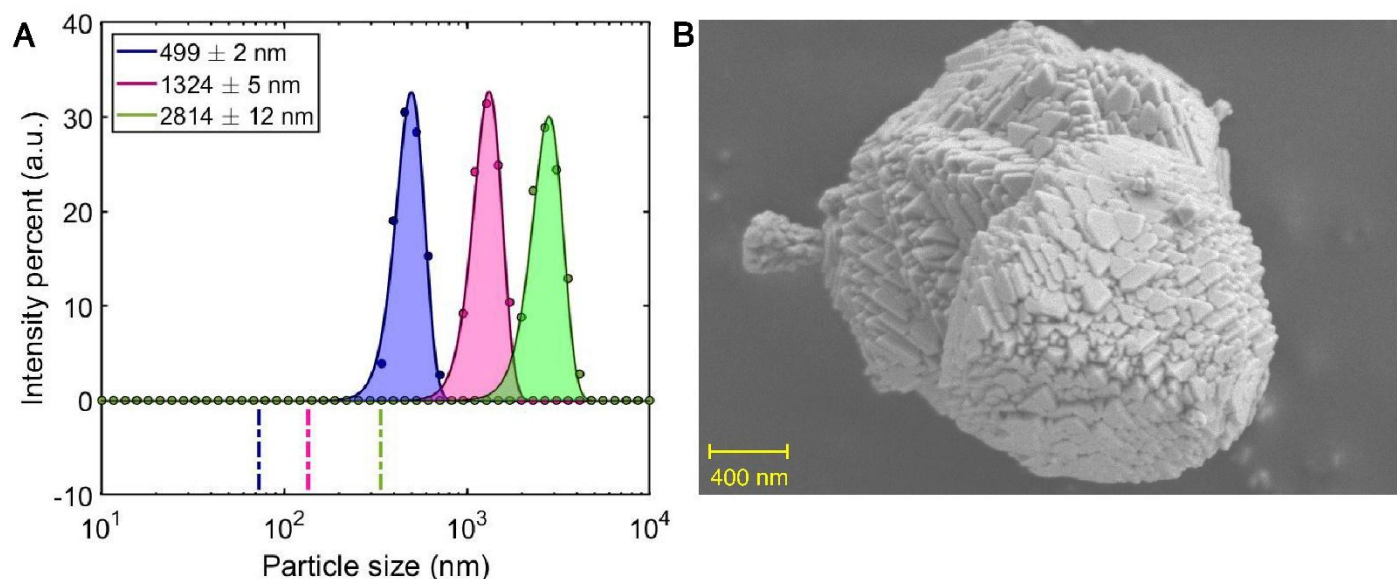


Fig. S2. (A) Particle size determination from DLS measurements. The maximum of the shaded region corresponds to the average secondary size as determined from the experiments. The dashed lines are the average primary particle sizes, as obtained from W-H analysis (shown in Fig. 2E of the main text). (B) An example SEM image representing both the primary as well as secondary particle sizes for the batch labeled in magenta in Panel-A.

But from the perspective of skyrmion physics, size of the primary particles is much more relevant compared to the secondary. Although the distribution appears to be narrow in panel B, an accurate particle size measurement cannot be obtained from the SEM images because particles are tilted, overlapping and/or partially embedded in the agglomerates. So, 3D particle size distribution cannot be obtained from SEM. We preferred to determine the primary particle size by performing Williamson-Hall (W-H) analysis. A large 2θ range is used such that the 3D particle size can be accurately obtained. As shown in the Fig. 2, the

primary particle size corresponding to the sample in the Panel B image is determined to be 136 ± 2 nm. Together with all the measurement protocols described above, we firmly believe in a tight distribution of the particle sizes, which correlates directly with the systematic behavior observed in the experimental magnetic properties.

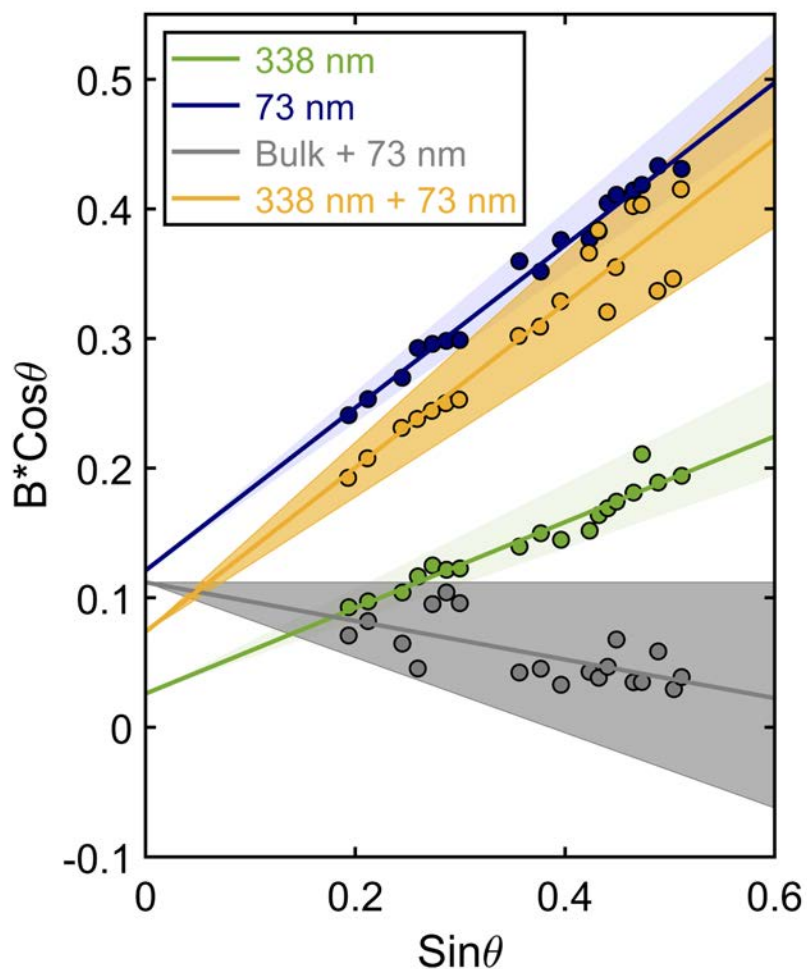


Fig. S3. Williamson-Hall measurements performed on a mixture of two particle sizes. Data for 338 nm and 73 nm have been shown for reference. The procedure to obtain the average particle height is identical to the ones described in the methods section.

In order to confirm the narrow size distribution, we performed some additional W-H measurements on a mixture made of 73 nm particles with 338 nm particles such that the size distribution becomes broad. Figure S3 shows that while the W-H plot for pure 73 nm and 338 nm samples are perfectly linear, a strong scattering is obtained at high 2θ angles for the mixture of 73 nm and 338 nm. Same broadening in the W-H plot is seen when the 73 nm particles are mixed with a powder obtained by crushing a Cu_2OSeO_3 single crystal. These additional measurements confirm the primary particle size distribution is narrow.

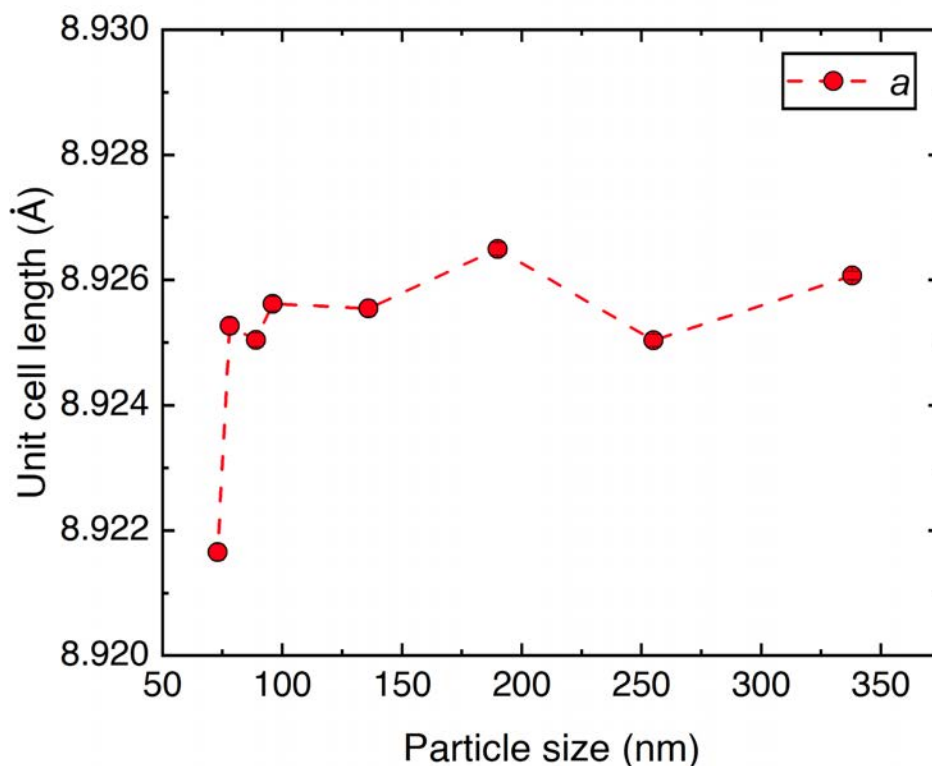


Fig. S4. Refinement of the powder patterns used for WH analysis. The obtained length of the unit cell lies very close to the reported value of 8.925 Å.

Transmission Electron Microscopy Studies. The crystallinity and structure of Cu_2OSeO_3 nanoparticles were investigated in selected area electron and high-resolution transmission electron microscopy (HRTEM). The as-fabricated Cu_2OSeO_3 nanoparticles were put into a solution of ethanol. The solution was then sonicated to break the aggregated nanoparticles and then using a micropipette, the solution of nanoparticles was drop cast onto TEM lacy carbon grids. The nanoparticles have a morphology of highly faceted cubic particles (as observed by SEM). Figure S5 (A) shows an example of such Cu_2OSeO_3 nanoparticle. Diffraction analysis was conducted on several particles, and investigation confirmed the high crystallinity and that particles were single crystals having Cu_2OSeO_3 structure. Fig. S5 shows the diffraction of a faceted cubic-shaped particle. The sample was tilted to the closest zone axis [311]. The diffraction pattern was simulated in the JEMS software¹. The calculation includes dynamical scattering effects for a 400 nm particle and the microscope coherence and electron beam illumination conditions. The JEMS simulation of selected areas electron diffraction pattern in Figure S5B shows excellent agreement for the Cu_2OSeO_3 crystal oriented on [311] zone axis.

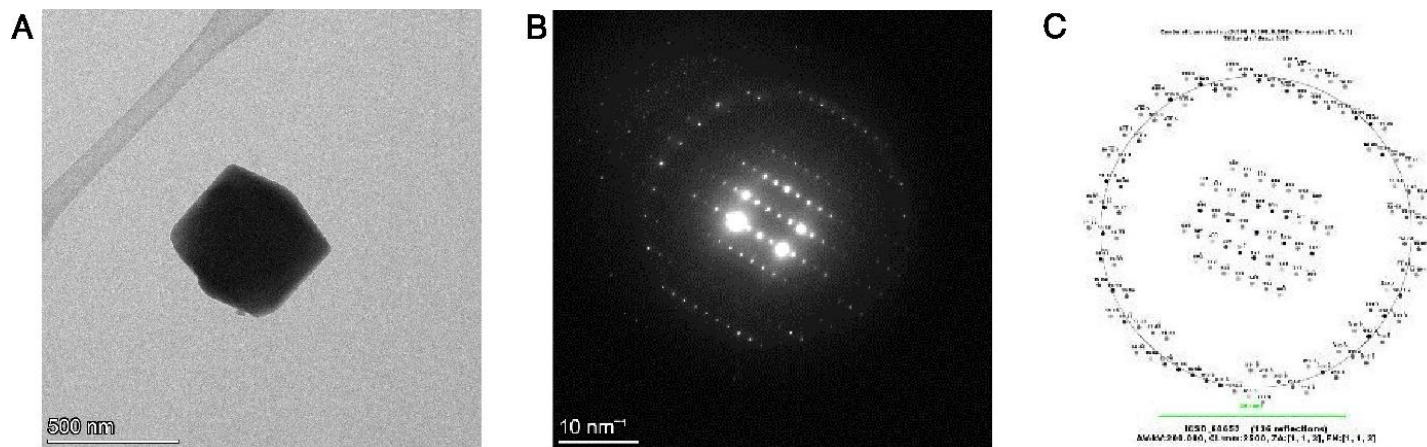


Fig. S5. (A) TEM image of faceted Cu_2OSeO_3 nanoparticle. (B) Experimental Selected Area Diffraction Pattern (SAED). (C) JEMS simulation of SAED of $[311]$ zone axis that includes zero and first order Laue zones.

High-resolution transmission electron microscopy (HRTEM) investigations were conducted using Thermo Fisher Scientific Talos TEM at 200kV accelerating voltage. Figure S6 shows HRTEM images taken from the edge region of the cubic shape Cu_2OSeO_3 nanoparticle shown in Fig. S5 (A) tilted on $[311]$ zone axis. We used the JEMS software package and performed a multi-slice simulation of the HRTEM image for 50 nm thick crystal on $[311]$ zone axis and the Talos microscope conditions were used to acquire images in Fig. S6 (A) and (B). The HRTEM simulation shows good agreement with the experimental HRTEM for defocus of 67 nm close to the Scherzer defocus (optimal) based on the aberration and coherence specifications of the Thermo Fisher Scientific Talos TEM. The SAED and HRTEM investigations confirm that Cu_2OSeO_3 nanoparticles are single crystals and do not have apparent defects.

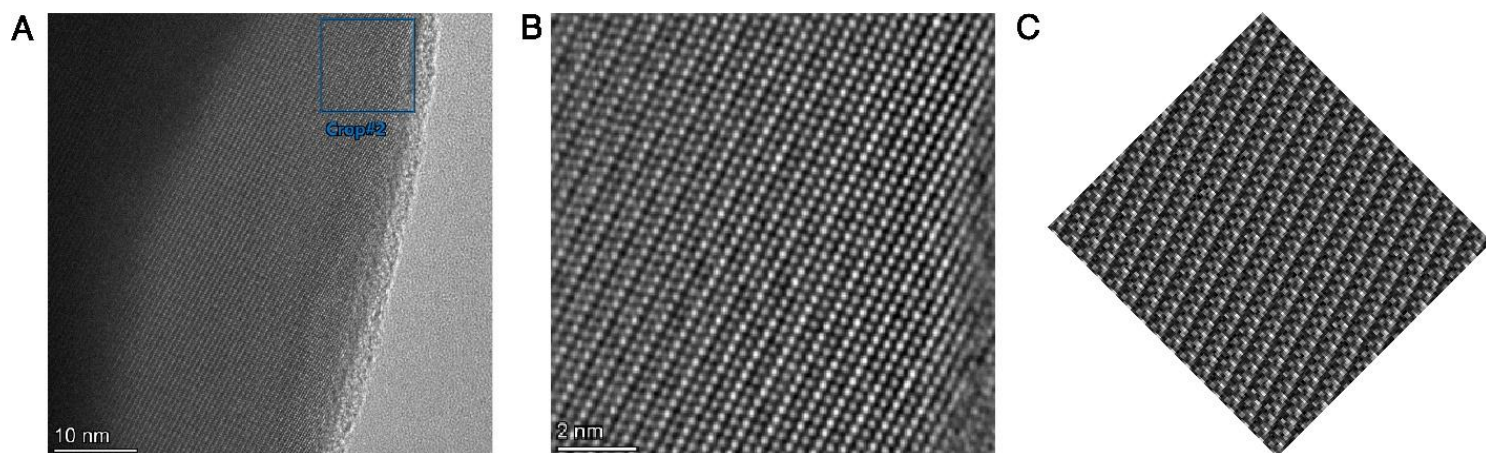


Fig. S6. (A) HRTEM image of the edge of Cu_2OSeO_3 nanoparticle in Fig. S5 (A) tilted to be aligned on $[311]$ zone axis. (B) higher magnification HRTEM image of area indicated by the blue in Fig S5 (A) showing atomic resolved lattice planes. (C) JEMS multi-slice calculation simulation of the Cu_2OSeO_3 nanoparticle with $[311]$ orientation and 50 nm crystal thickness.

Magnetometry. AC susceptibility field scans were performed for sample of all particle sizes at constant temperatures (Fig. S7A-G), in a similar manner to those shown in Fig. 3C, F, and I. Since the contour plots are created out of the imaginary component of the total susceptibility, a rather growing dissipative region can be observed close to T_c , for reduced particle size. Motivated by this, AC susceptibility temperature scans were performed at constant magnetic fields as shown in Fig. S8. Strong correlations among the chiral fluctuations close to T_c , drive the HM-transition to lower temperatures in bulk- Cu_2OSeO_3 .

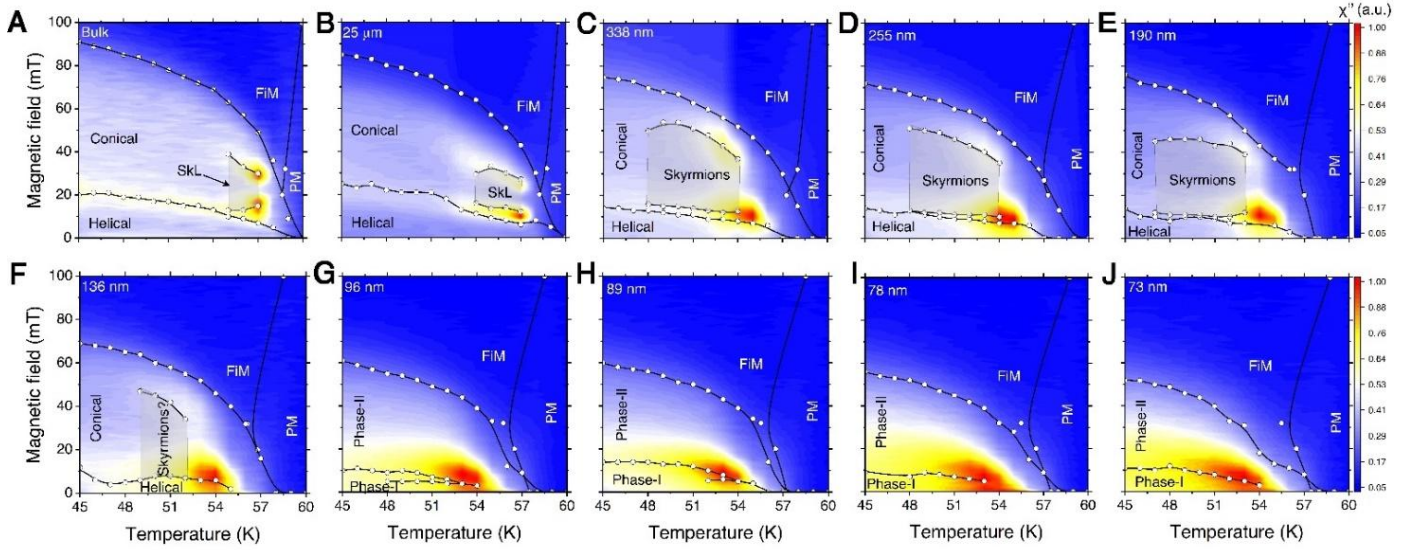


Fig. S7. (A)-(J) display the magnetic phase diagrams of all particle sizes considered in the text. Panel A, C and J are already shown in Fig.3 of the main text. The phase boundaries have been extracted from the AC susceptibility measurements, following similar protocols as shown in Fig. 3B, E and H of the main text.

The divergence in the susceptibility close to T_c for smaller particles signifies a direct consequence of finite-size effects. Similar results were obtained with 100 mT of applied magnetic field (Fig. S8E), suggesting the applicability of these finite-size effects not only in zero-field transitions, but also finite-field crossovers. In bulk- Cu_2OSeO_3 , temperature-cooling scan in presence of 20 mT magnetic field drives the system through $\text{PM} \rightarrow \text{SkL} \rightarrow \text{Con.}$ phase, represented by the cusp in the susceptibility data (Fig. S8D). In the absence of a well-defined lattice of skyrmions, this cusp vanishes in the particles. In the biggest particles, a small change in the susceptibility can be seen. These changes are thus attributed to the presence of few skyrmion tubes and/or chiral bobbles. Whereas, in the smallest particles, absence of this feature not only disfavors the possibility of having skyrmion tubes but also completely agrees with the SANS observations.

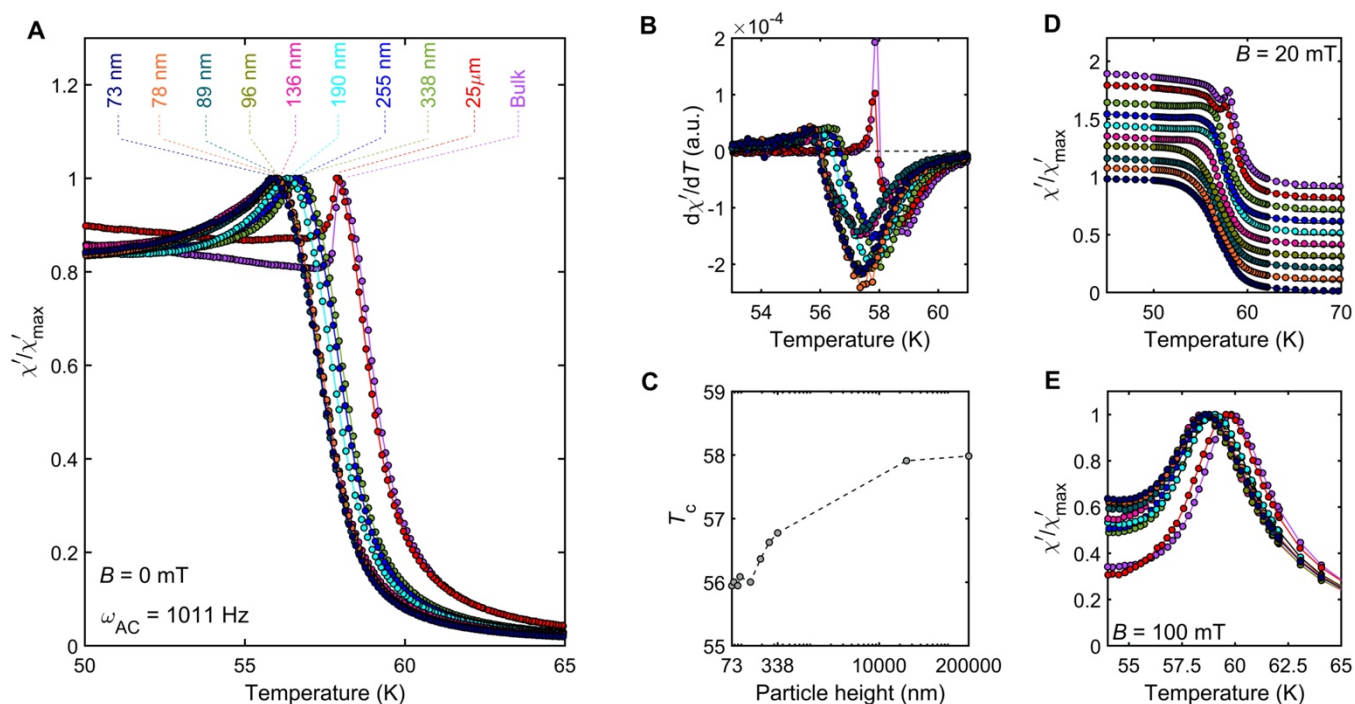


Fig. S8. (A) Zero-field AC susceptibility temperature scans for all the particles. In order to emphasize the fact that T_c decreases with decreasing particle size, all the scans have been normalized with respect to the maximum. (B) shows the differentiation with respect to temperature for all the scans shown before, thus extracting the T_c . (C) The estimated T_c from the previous procedure compared with all particle sizes considered. AC susceptibility temperature scan in presence of (D) 20 mT and (E) 100 mT of DC magnetic field, also for all the particles.

Small angle neutron scattering. SANS measurements for the biggest particles (338 nm) shed more lights on the magnetic phases established in Fig. 5A-F of the main text. In order to suppress the issue of multiple scattering, a pellet of thickness less than 0.5 mm was used in a custom-made Al-holder. Firstly at 53 K in presence of zero magnetic field, as shown in Fig. S9A, the detector image shows an isotropic scattering ring around $Q = 0$. This scattering pattern may be the result of helical spin textures within each of the randomly oriented octahedron of Cu_2OSeO_3 . The $|q|$ of this scattering pattern, analyzed with a Pseudo-Voigt function, closely matches with the one obtained previously from bulk- Cu_2OSeO_3 . In contrast, for the smallest nanoparticles (73 nm), $|q|$ was found to be around $0.087(1) \text{ nm}^{-1}$. In real space, this closely follows the entire height of the octahedron particles, thus outlining the main effects of confinements due to reduced crystallite size. The evolution of this $|q|$ with external magnetic field suggests that the pitch length slowly relaxes to the bulk limit before vanishing in the field-polarized state.

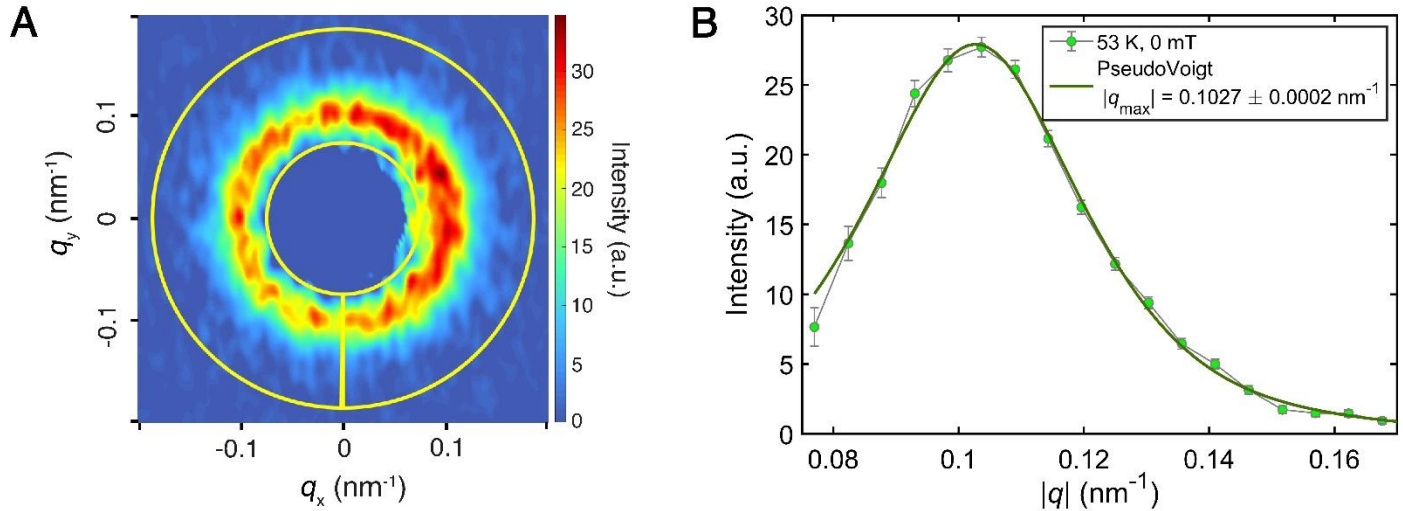


Fig. S9. (A) SANS detector image for 338 nm particles at 53 K at zero magnetic field. In order to estimate the total radial intensity evolution as a function of $|q|$, an isotropic sector was chosen as shown in yellow. To ensure all magnetic scattering is considered for this analysis, the width of the sector was chosen such that it spans the maximum of the detector image. (B) magnetic scattering as a function of q extracted from the sector box defined in (A). The green solid line represents a Pseudo-Voigt fit to the same.

We note that a single period helical spiral can also produce a “two-spot” SANS pattern, as shown in Fig. S11. Here, we demonstrate the single 73 nm helical pitch embedded into the octahedron with 73 nm height, and the corresponding two-dimensional fast Fourier transform (FFT) of the m_z -component of the magnetization. This FFT pattern can serve as a rough approximation of the SANS intensity map in the (yz) plane, where the neutron beam k_i is parallel to x and helical propagation axis is parallel to y [D. A. Gilbert, *et al.* Physical Review Materials 3.1 (2019): 014408]. Two bright spots, corresponding to the magnetic structure factor are clearly observed in the FFT (Fig. S11B). The possible emergence of aperiodic arrangements of magnetic skyrmions, chiral bobbles, merons or other isolated textures embedded into ferromagnetic background should be manifested in form-factor small-angle scattering across the large Q -range [L. G. Vivas, *et al.* Physical Review Letters 125.11 (2020): 117201]. With the present dataset at hand we are not able to discuss this weak effect due to the limited dynamic range, and predominance of the peaked scattering intensity.

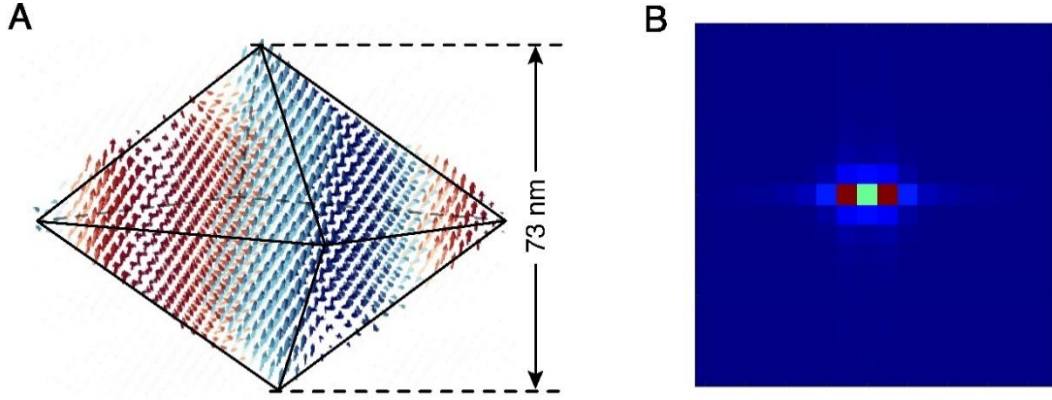


Fig. S11. (A) A single period of magnetic helix embedded into 73 nm nanoparticle. (B) Fast-Fourier transform of the z -component of the magnetization projected on the (yz) plane, showing characteristic “two-spot” pattern.

Micromagnetic simulations. The magnetization M component along the direction of the applied field was extracted from the simulations for both $B \parallel [001]$ (along the particle height, as seen in Fig. 7A) and $B \parallel [111]$ (along the particle facet, in Fig. 7B). Metamagnetic transitions seen in both $M(B)$ and dM/dB graphs illustrate the evolution of magnetic textures shown in Fig. 6.

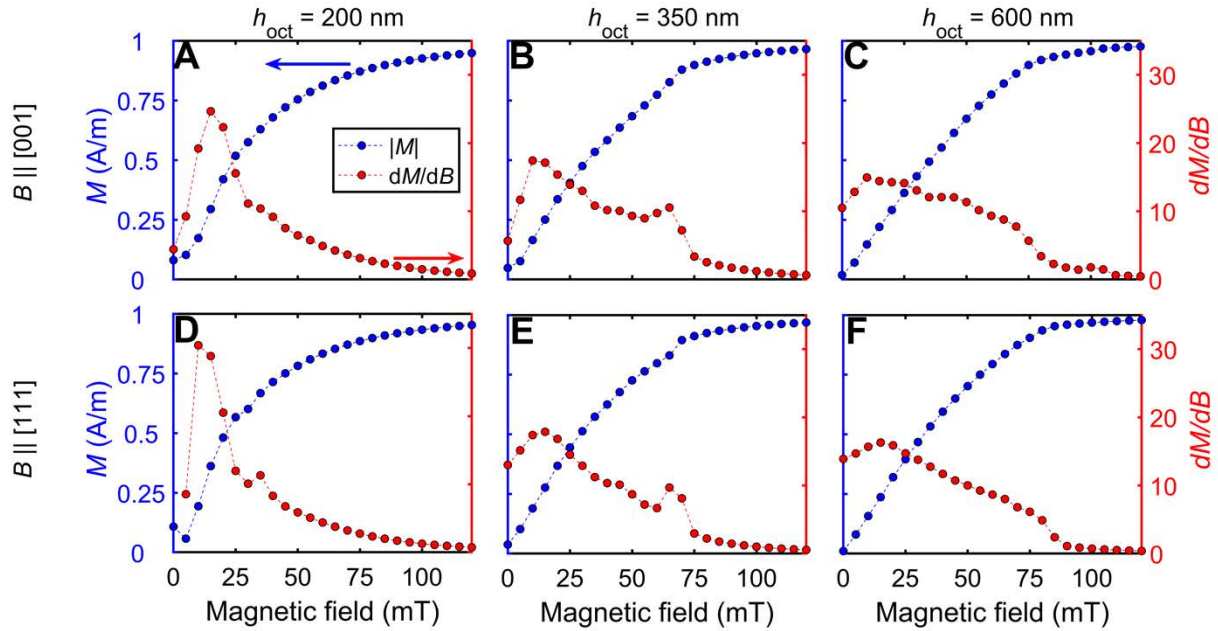


Fig. S12. For the three sizes shown in Fig. 6, evolution of the total magnetization as a function of magnetic field, as obtained from micromagnetic simulations. Total magnetization refers to the norm of the three spatial components. (A)-(C) represent when the magnetic field was applied along the top vertex of the octahedron ($[100]$), whereas (D)-(F) represent those along one of the facets ($[111]$). dM/dB clearly shows the metamagnetic-type transitions in individual nanoparticles (for example, panel B).